

UC Berkeley

UC Berkeley Previously Published Works

Title

Structural and Compositional Factors That Control the Li-Ion Conductivity in LiPON Electrolytes

Permalink

<https://escholarship.org/uc/item/1f76v45v>

Journal

Chemistry of Materials, 30(20)

ISSN

0897-4756

Authors

Lacivita, Valentina
Artrith, Nongnuch
Ceder, Gerbrand

Publication Date

2018-10-23

DOI

10.1021/acs.chemmater.8b02812

Peer reviewed

Structural and Compositional Factors That Control the Li-Ion Conductivity in LiPON Electrolytes

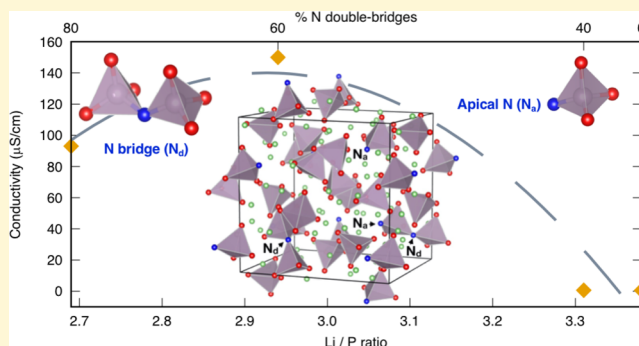
Valentina Lacivita,^{*,†,‡} Nongnuch Artrith,^{‡,§} and Gerbrand Ceder^{*,†,‡}

[†]Materials Science Division, Lawrence Berkeley National Laboratory, Berkeley, California 94720, United States

[‡]Department of Materials Science and Engineering, University of California, Berkeley, Berkeley, California 94720, United States

S Supporting Information

ABSTRACT: Amorphous Li-ion conductors are important solid-state electrolytes. However, Li transport in these systems is much less understood than for crystalline materials. We investigate amorphous LiPON electrolytes via *ab initio* molecular dynamics, providing atomistic-level insight into the mechanisms underlying the Li⁺ mobility. We find that the latter is strongly influenced by the chemistry and connectivity of phosphate polyanions near Li⁺. Amorphization generates edge-sharing polyhedral connections between Li(O,N)₄ and P(O,N)₄, and creates under- and overcoordinated Li sites, which destabilizes the Li⁺ and enhances their mobility. N substitution for O favors conductivity in two ways: (1) excess Li accompanying 1(N):1(O) substitutions introduces extra carriers; (2) energetically favored N-bridging substitutions condense phosphate units and densify the structure, which, counterintuitively, corresponds to higher Li⁺ mobility. Finally, bridging N is not only less electronegative than O but also engaged in strong covalent bonds with P. This weakens interactions with neighboring Li⁺ smoothing the way for their migration. When condensation of PO₄ polyhedra leads to the formation of isolated O anions, the Li⁺ mobility is reduced, highlighting the importance of oxygen partial pressure control during synthesis. This detailed understanding of the structural mechanisms affecting Li⁺ mobility is the key for optimizing the conductivity of LiPON and other amorphous Li-ion conductors.



1. INTRODUCTION

Lithium phosphorus oxynitride (LiPON) is a solid Li-ion conductor of general formula Li_xPO_yN_z. Amorphous LiPON has been widely used as electrolyte in thin-film rechargeable batteries since the pioneering work of Bates and co-workers at the Oak Ridge National Laboratory.¹ The reason for the success of LiPON thin-film electrolytes, usually sputter deposited to a thickness of 1 μm, is that they conjugate fairly good room-temperature ionic conductivity (2–3 μS/cm, activation energy $E_a \approx 0.55$ eV), high electronic resistivity ($>10^{14}$ Ω cm), a wide electrochemical window, and so far unmatched long-term durability in terms of cycling performance and storage.^{1–5} Experiments have shown that LiPON can withstand thousands of charge–discharge cycles in contact with metallic Li and transition metal cathodes at cell potentials up to above 5 V against Li, without displaying signs of degradation in cycling performance or dendrite formation.

Although no conclusive explanation has yet been given for the outstanding electrochemical performance of LiPON, it is commonly believed that this relates to the presence of N in the structure. Indeed, it was the observation that nitriding alkali phosphate glasses improves their mechanical and chemical resistance^{6–8} that originally motivated investigations on LiPON as a possible electrolyte.⁹ Likewise, N incorporation into phosphate structures, whether they are bulk glasses or

amorphous thin films, is often indicated as a factor enhancing the ionic conductivity σ .^{9–12}

The ionic conductivity of LiPON thin films increases significantly (while the activation energy for Li diffusion decreases) with the atom percentage (at. %) of N incorporated in the structure: impedance measurements by Bates et al.¹⁰ showed more than a factor 45 increase in σ at 25 °C when increasing the N content from 0 at. % ($\sigma = 7 \times 10^{-8}$ S/cm) to 6 at. % ($\sigma = 3.3 \times 10^{-6}$ S/cm). The cause of this improvement in ionic conductivity via nitridation is not fully understood, but different suggestions have been put forward. The invoked arguments are essentially of two types, either structural or electrostatic, both of which have been substantiated by parallels with the well-studied case of bulk nitrided metaphosphate glasses,^{6–9,13–15} although caution is warranted due to considerable differences in reacting materials and processing route.¹⁶

The structural argument relies on the idea that nitridation promotes cross-linking via formation of doubly (N_d) and triply coordinated (N_t) N bridges among P atoms. It is assumed that the increase in cross-linking density of the amorphous network

Received: July 4, 2018

Revised: September 13, 2018

Published: September 15, 2018

with N content implements the “mixed anion effect”^{17–19} of promoting Li-ion mobility by providing interconnected, but as yet unspecified, conduction pathways with low activation energy. This explanation was first suggested by Bates et al.,^{1,10} who resolved N_{1s} X-ray photoelectron spectroscopy (XPS) data collected on LiPON thin films in contributions from doubly and triply coordinated N atoms, along the lines of previous work on bulk nitrided glasses.¹⁴ However, it is worth noting that a different interpretation was given to very similar N_{1s} XPS features reported shortly thereafter for polycrystalline Li_{2.88}PO_{3.73}N_{0.14},²⁰ where diffraction and chromatography data hinted instead to most of the N forming isolated PO₃N units (with apical N, N_a) and only a small fraction of N_d bridges due to some Li ↔ P disorder in the structure.

The electrostatic argument refers to the higher covalency of P–N bonds with respect to P–O, which would result in a reduction of the overall electrostatic interaction with Li⁺, translating in a lower activation energy and hence higher ionic conductivity.^{9,21,22} Contradicting this point, Unuma and Sakka²¹ argued that due to the formation of strong P–N and P=N connections, the increase in structural density and network-strain energy²³ with N content should increase the activation energy for ionic diffusion. In fact, experimental evidence collected on phosphate glasses indicates that incorporation of high N contents affects the Li coordination as seen by nuclear magnetic resonance (NMR),¹⁵ suggesting the intensification of Li–O interactions as a factor counteracting the increase in ionic conductivity promoted by other mechanisms.

Thus, the effect of N incorporation on the lithium phosphate structure and conductivity mechanism remains controversial. Understanding in detail how N incorporation modifies the local structure and enhances conductivity would give guidance on how to improve the conductivity of other oxide electrolytes. In this paper we report an *ab initio* investigation of the role of composition and structural changes in affecting the ionic conductivity of amorphous LiPON electrolytes. Previously, Du and Holzwarth^{24–26} performed density functional calculations on crystalline materials related to LiPON. Reference 24 investigated the effect on the Li⁺ migration of isolated defects, such as O vacancies and N substitutions, introduced into crystalline Li₃PO₄ and found that the bridging N_d configuration is preferred by nearly 3 eV relative to N_a. These authors also noticed that while N_a and N_d tend to trap vacancies and interstitial Li⁺ ions, migration barriers in their neighborhood are as small as 0.4–0.6 eV, so that one could extrapolate to relatively low migration energies ($0.7 \lesssim E_m \lesssim 1.0$ eV) for appreciable concentrations of such defects.

We use *ab initio* molecular dynamics (AIMD) to generate LiPON amorphous structure models and study Li⁺ diffusion in them. The atomistic approach of this work allows us to break down the complexity of the electrical behavior of LiPON electrolytes into its determining factors and provide concrete elements to explain the mechanisms underlying their ionic conductivity. With the goal of discerning the relationship between structure and electrical behavior of LiPON electrolytes, we systematically investigate the effect on ion conduction of different factors, namely the amorphous framework, the Li content, and the presence of N in both bridging and nonbridging configurations. By comparing first the behavior of amorphous lithium phosphate, a-Li₃PO₄, against its crystal form, γ-Li₃PO₄, we demonstrate the importance of the amorphous character in enhancing the mobility of the charge

carriers as a result of the modification of the Li⁺ environment. We also verify that excess Li introduced by doping a-Li₃PO₄ has in itself a beneficial effect on the ionic conductivity. Finally, we analyze the specific role of N in modifying the nature of cation–anion interactions within the structure.

Our computed amorphous LiPON structures display N in N_a and N_d configurations, the latter being confirmed as energetically favored, whereas no triple N_t bridges are found. This is consistent with the experimental structure characterization of polycrystalline LiPON by Wang et al.²⁰ and with first-principles calculations suggesting contributions from N_a species in the N_{1s} XPS absorptions of amorphous LiPON.^{27,28} While no privileged pathways are recognized in support of the speculations about the “mixed anion effect”, we find that N_d bridges favor the diffusion of Li⁺ because the saturation of the bond valence of N via strong covalent interactions with P limits the Li–N interactions. Nonetheless, such effect can be countered by strong Li–O interactions when the condensation into N_d bridges causes the release of isolated O anions in the structure.

2. METHOD

2.1. Generation of Amorphous Structure Models and Diffusivity Simulations. The amorphous structure models discussed in the present work and the corresponding ionic conductivities have been obtained via AIMD simulations. AIMD simulations are performed with the projector augmented-wave approach²⁹ and the Perdew–Burke–Ernzerhof (PBE)³⁰ generalized-gradient approximation to the density functional theory (DFT) as implemented in the Vienna *ab initio* simulation package (Vasp).³¹ To keep the computational cost reasonable, we adopted a minimal Γ -only k -point grid. The AIMD time step was set to 2 fs, and the temperature of the system was controlled by periodic velocity rescaling (Berendsen thermostat) every 50 or 100 steps. Despite some well-known limits in the description of temperature fluctuations, this thermostat has been shown to provide reliable dynamic properties,³² which are those of interest here.

To generate amorphous structures, we used unit cells containing 118–134 atoms. Initial structure guesses were set either by applying the optimized atom packing procedure developed in the software Packmol³³ or by using DFT-relaxed near-ground-state defect crystal structures generated as explained in section 2.2. In the first case, we inserted atoms in a cubic box with density ρ about 75–80% the experimental reference for amorphous Li₃PO₄ (i.e., $\rho = 2.2$ g/cm³), and performed a simulated annealing from 3000 to 0 K, reducing the temperature by steps of 500 K at a rate of 250 K/ps. In the second case, we adopted a melt-and-quench protocol in which the initial crystalline structure (relaxed to its minimum-energy volumetric density ρ) is first melted at 3000 K and then cooled via the previously described simulated annealing. At each step of both melt-and-quench and annealing simulations the system is allowed to equilibrate for at least 10 ps. All these AIMD simulations were performed at constant volume, and the latter was resized isotropically (i.e., by variations of ± 0.1 Å along each Cartesian direction) at intervals during the equilibration so as to counterbalance the calculated total pressure. The energy cutoff for these calculations was set to 300 or 400 eV. For the optimization of atomic positions and cell parameters at 0 K, we used an energy cutoff of 520 eV and a Γ -centered Monkhorst–Pack k -point grid with density 1000/(number of atoms in the unit cell). Pair distribution functions, $G(\vec{r})$ (Å^{–2}),

of the DFT optimized amorphous structure models were computed using the library *sreal* developed in the software package DiffPy³⁴ for the study of the atomic structure of materials. Structure drawings were produced using the software Vesta.³⁵

To determine the Li⁺ mobility, we performed AIMD simulations at constant volume and temperature T between 700 and 1300 K for at least 100 ps. The high temperatures are required to speed up Li⁺ diffusion and thus reduce the simulation time. Ionic conductivities σ are calculated as

$$\sigma = \frac{N_{\text{Li}} e^2}{V k_{\text{B}} T} D \quad (1)$$

with e the elementary charge and k_{B} the Boltzmann constant. D is obtained from the net Li-ion motion:

$$D = \frac{1}{6 N_{\text{Li}}} \lim_{t \rightarrow \infty} \frac{1}{t} \left\langle \left| \sum_{i=1}^{N_{\text{Li}}} [\vec{r}_i(t) - \vec{r}_i(0)] \right|^2 \right\rangle \quad (2)$$

where $r_i(t)$ is the instantaneous position of the i th Li ion and the angular brackets indicate ensemble averaging over initial configurations. When Li ions are the only mobile charge carriers, eq 1 is equivalent to the Green–Kubo correlation function for electrical conductivity, which takes into account cross-particle correlations.^{36–39} Indeed, D in eq 2 includes both the independent Li-ion contribution

$$\Delta_{\text{self}}(t) = \frac{1}{N_{\text{Li}}} \sum_{i=1}^{N_{\text{Li}}} |\vec{r}_i(t) - \vec{r}_i(0)|^2 \quad (3)$$

and the interaction between different Li ions, namely

$$\Delta_{\text{cross}}(t) = \frac{1}{N_{\text{Li}}} \sum_{i=1}^{N_{\text{Li}}} \sum_{j \neq i=1}^{N_{\text{Li}}} [\vec{r}_i(t) - \vec{r}_i(0)] \cdot [\vec{r}_j(t) - \vec{r}_j(0)] \quad (4)$$

Equation 3 defines the mean-square displacement (MSD) of Li⁺ over time t , which is related to the self-diffusion or tracer diffusion coefficient D^* as follows:

$$D^* = \frac{1}{6} \lim_{t \rightarrow \infty} \frac{\langle \Delta_{\text{self}}(t) \rangle}{t} \quad (5)$$

In practice, at each T , the values of D^* and D are obtained from a linear fitting of the displacement terms $\Delta_{\text{self}}(t)$ and $[\Delta_{\text{self}}(t) + \Delta_{\text{cross}}(t)]$ vs t , using the maximum smoothing technique implemented in the Python Materials Genomics (pymatgen) toolkit^{40–42} and averaging over trajectory intervals of 30 ps. No melting transitions take place in this time scale, as verified from the root-mean-square displacement (RMSD) of the P atoms (center of the phosphate tetrahedra) being of the order of 1–2 Å at the highest temperatures. Li-ion displacements are calculated with respect to the center-of-mass of the framework, which includes all non-Li ions. Room-temperature conductivities and activation energies are extracted from Arrhenius plots of D .

To characterize the spatial and temporal distribution of the Li ions, we calculated the van Hove self-correlation function:⁴³

$$G_s(\vec{r}, t) = \frac{1}{N_{\text{Li}}} \sum_{i=1}^{N_{\text{Li}}} \langle \delta(\vec{r} - |\vec{r}_i(t) - \vec{r}_i(0)|) \rangle \quad (6)$$

where δ is the Dirac delta function. $G_s(\vec{r}, t)$ defines the probability distribution that at time t an ion is found at a distance r from its initial position.

2.2. Calculation of Defect Formation Energies for N-Doped Lithium Phosphate. Besides AIMD simulations, static energy calculations have also been performed to characterize the energetics of different types (and concentrations) of N defects in crystalline Li₃PO₄. Defect formation energies for the insertion of N into Li₃PO₄ are estimated using N-doped near-ground-state crystal structures identified through the combination of a genetic-algorithm (GA) and machine-learning potential (MLP) energy calculations. Details about the coupled GA-MLP method can be found elsewhere.⁴⁴ In short, this approach serves as a computationally optimized method for sampling potential energy surfaces and can be outlined as follows: (i) a number of N-doped crystal structure configurations is generated with the GA, starting from a supercell of Li₃PO₄ with 16 formula units (128 atoms); (ii) the energies of these defected structures are calculated using a specially trained MLP for fast screening; (iii) the 30 structures with lowest energy among those sampled with the MLP are selected and their energy accurately recalculated at the DFT-PBE level; and (iv) the structure with the lowest DFT energy is then reinjected at the beginning of the GA process to generate new configurations, and the process restarts until the convergence criteria are met.

All MLP simulations were performed using the *atomic energy network* package.⁴⁵ We employed an atomistic MLP based on artificial neural networks (ANN) with two hidden layers and each 15 nodes with hyperbolic tangent activation functions. A Chebyshev expansion of the radial and angular distribution functions with 18 basis functions each (giving a total descriptor size of 36) was used to map the local atomic environment,⁴⁶ so that the total number of ANN weights is 811. The MLP was trained on the DFT energy of around 20000 LiPON related structures and cross-validated on an independent test set comprising 2200 additional structures, giving a root-mean-squared error of 7.15 meV/atom and a mean absolute error of 5.31 meV/atom relative to the DFT reference energies (see Figure S1 in the Supporting Information). The corresponding training set errors are 5.27 and 4.60 meV/atom.

All low-energy structure models identified with the GA-MLP approach for different types and concentrations of N defects have been fully relaxed at the DFT level and then used to calculate the defect formation energies discussed in what follows. Some of these DFT-relaxed near-ground-state defected structures have also been used as initial guesses for the AIMD melt-and-quench process described in section 2.1 for the generation of amorphous LiPON structures with the same composition.

2.3. Exploration of the Compositional Space of LiPON Compounds. Li_xPO_yN_z compounds can be mapped onto a multidimensional compositional space as represented in the phase diagram in Figure 1. Typical compositions of amorphous LiPON electrolytes display coefficients $x \approx 3$, $z < 0.5$, and $3 < (y + z) < 4$, which place them close to the stoichiometry of the orthophosphate precursor, Li₃PO₄, normally used as sputtering target. Occasionally, crystalline LiPON samples have also been synthesized by solid-state reaction, e.g., Li_{2.88}PO_{3.73}N_{0.14} from a mixture of Li₃N and LiPO₃²⁰ and Li₂PNO₂ from a mixture of Li₂O, P₂O₅, and P₃N₅.⁴⁷

Assuming that all N enters the Li_xPO_yN_z structure as N^{3−}, charge balance requires that $x = 2y + 3z - 5$. This condition

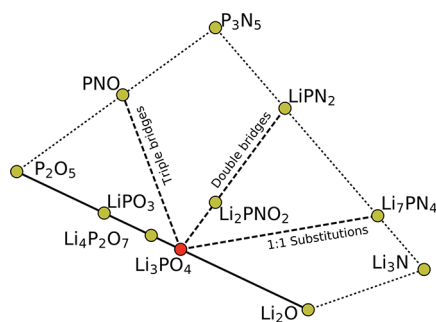


Figure 1. Phase diagram showing relevant LiPON-related compositions in the $\text{Li}_x\text{PO}_y\text{N}_z$ space. While normal bulk oxynitrided phosphate glasses are obtained from LiPO_3 melts, amorphous LiPON thin films are usually fabricated by radio-frequency magnetron sputtering of Li_3PO_4 targets. Starting from the Li_3PO_4 stoichiometry, N substitutions might occur along and between three binaries indicated by the dashed lines, i.e., Li_3PO_4 – Li_7PN_4 , Li_3PO_4 – LiPN_2 , and Li_3PO_4 – PNO . See the text for details.

signifies that the composition of LiPON electrolytes is determined not only by the amount of N doping but also by the anions to P ratio, which depends on whether N for O substitutions in Li_3PO_4 lead to the condensation of phosphate tetrahedra.

Spectroscopic studies^{1,10,20} suggest that N can be present in both apical (N_a) and bridging configurations—either doubly coordinated (N_d) or triply coordinated (N_t) by P atoms, which are schematically represented in Figure 2. Hence, we

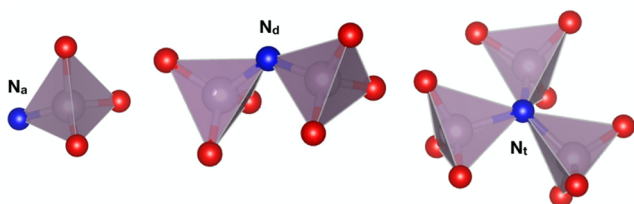


Figure 2. Schematic representation of possible N configurations in phosphate structures: apical N (N_a), double bridging N (N_d), and triple bridging N (N_t). Color code: N (blue), P (gray), and O (red).

distinguish three types of N for O substitution that may take place in Li_3PO_4 , the corresponding pathways being indicated by the dashed lines in the phase diagram in Figure 1: (1) N_a is

formed by a simple 1N:1O substitution, i.e., $(\text{N}^{3-} + \text{Li}^+) \leftrightarrow \text{O}^{2-}$, which leaves the $(\text{O} + \text{N}):\text{P}$ ratio constant at 4 and is accompanied by the insertion of excess Li^+ along the binary Li_3PO_4 – Li_7PN_4 . (2) N_d bridges are formed by $\text{N}^{3-} \leftrightarrow (2\text{O}^{2-} + \text{Li}^+)$ substitutions, which generate deficiencies in both Li and anion contents with respect to the Li_3PO_4 reference. Full 1- and 3-dimensional double-bridging condensations lead to compositions Li_2PNO_2 and LiPN_2 , respectively. (3) N_t bridges are formed along the binary Li_3PO_4 – PNO by $\text{N}^{3-} \leftrightarrow (3\text{O}^{2-} + 3\text{Li}^+)$ substitutions, which again entail a decrease in the $(\text{O} + \text{N}):\text{P}$ ratio ($y + z < 4$) as well as in Li content. In addition to N for O substitutions into Li_3PO_4 , Li and anion contents may be modified also by incorporation of extra Li_2O (or Li_3N) in the structure, which would shift the composition to the lower right side of the phase diagram.

Hence, it is seen that there are at least three independent compositional variables associated with the incorporation of N into Li_3PO_4 , and these are the Li content, the N content, and the ratio $(\text{O} + \text{N}):\text{P}$. To assess their impact on the electric behavior of LiPON electrolytes, in this work we have generated and studied various amorphous models with stoichiometries that reflect variations across all three axes while remaining close to experimental compositions. Specifically, we will consider compositions with 3.7–4.5 at. % N and different anion to P ratios to explore the potential of condensation between phosphate units along with the presence of Li excess or deficiencies.

3. RESULTS

Table 1 summarizes ionic conductivities and activation energies calculated for the various amorphous LiPON structure models produced for this work. Experimental data^{4,48,49} collected on amorphous LiPON electrolytes are reported for comparison.

We note that the agreement between calculated and experimental data is generally fairly good. Differences might be explained with the limits of the computational model (e.g., short length and time scales), the slow convergence of the diffusion coefficients with the simulation time, and the uncertainty associated with fitting displacement terms vs time data and extrapolating the room-temperature diffusivity from much higher temperatures. However, in the following we will rather focus on the relative comparison between the calculated structures, by investigating separately the effect of

Table 1. Diffusivity Coefficients D (cm^2/s), Conductivities σ (S/cm), and Activation Energies E_a (meV) Extrapolated at Room Temperature for Amorphous Structure Models from AIMD Simulations and Corresponding Atomic Percentage of N (at.% N), Number of Apical N ($\# \text{N}_a$), Number of Double Bridging N ($\# \text{N}_d$), and Density ρ (g/cm^3); Experimental Data on Amorphous Electrolytes Are Reported at the Bottom for Comparison

	at. % N	$\# \text{N}_a$	$\# \text{N}_d$	ρ	D	σ	E_a
computed							
$\text{Li}_{2.69}\text{PO}_{3.38}\text{N}_{0.31}$	4	1	4	2.04	5×10^{-10}	9.3×10^{-5}	447
$\text{Li}_{2.94}\text{PO}_{3.50}\text{N}_{0.31}$	4	2	3	2.33	7×10^{-10}	1.5×10^{-4}	405
$\text{Li}_{3.31}\text{PO}_{3.69}\text{N}_{0.31}$	4	3	2	2.30	3×10^{-12}	6.6×10^{-7}	560
$\text{Li}_{3.38}\text{PO}_{3.62}\text{N}_{0.38}$	5	6	0	2.31	2×10^{-12}	5.6×10^{-7}	570
experimental							
$\text{Li}_{2.7}\text{PO}_{3.9}$ ¹	0					7.0×10^{-8}	670
$\text{Li}_{2.9}\text{PO}_4$ ^{49,50}	0				6×10^{-13}	$2\text{--}4 \times 10^{-7}$	550–580
$\text{Li}_{3.1}\text{PO}_{3.8}\text{N}_{0.16}$ ⁴	2					2.0×10^{-6}	570
$\text{Li}_{3.3}\text{PO}_{3.8}\text{N}_{0.22}$ ⁴	3					2.4×10^{-6}	560
$\text{Li}_{2.9}\text{PO}_{3.3}\text{N}_{0.46}$ ⁴	6					3.3×10^{-6}	540

amorphization, excess Li and N doping on the Li-ion conductivity.

3.1. Effect of Amorphization. There are two well-characterized crystalline forms of Li_3PO_4 which are labeled β and γ . Both have orthorhombic cells with isolated phosphate units whose relative orientation distinguishes the two polymorphs. Here we will focus on the γ form, which is the one usually adopted as target in the magnetron sputtering process for synthesizing LiPON thin films.

Ivanov-Shitz et al.⁵¹ measured the ionic conductivity of γ - Li_3PO_4 to be $\sigma = 4.2 \times 10^{-18}$ S/cm ($E_a = 1.2$ eV), which is about 10 orders of magnitude smaller than the room-temperature conductivity measured for the amorphous phase, a- Li_3PO_4 ($\sigma \approx 10^{-8}$ – 10^{-7} S/cm, $E_a = 550$ – 670 meV).^{1,48,49} In line with these experimental data, recent molecular dynamics calculations using a machine-learning-based DFT-trained neural network potential to allow for long time scale simulations provided an effective activation energy for a- Li_3PO_4 of 590 meV.⁵² In confirmation of the extremely poor ionic conductivity of γ - Li_3PO_4 , Du and Holzwarth⁵³ calculated activation energies on the order of 1–1.3 eV, which include an important contribution from the formation energy of interstitial and vacancy defects. They also noticed that the introduction of interstitial Li defects should provide the most efficient ion transport mechanism, with migration barriers obtained from nudged elastic band calculations as small as 0.3 eV. As for our calculations, an AIMD trajectory of 120 ps was not enough to reach appreciable MSD of Li^+ ions in γ - Li_3PO_4 , even at high temperatures (1100 K), which is consistent with very low intrinsic Li-ion conductivity in γ - Li_3PO_4 .

For our amorphous structure model we have adopted the perfect Li_3PO_4 stoichiometry, although compositions reported for lithium phosphate thin films are often off-stoichiometric^{1,50,54} due to the loss of Li_2O or the introduction of excess Li_2O during the synthesis process. We avoided such compositional defects to better deconvolute the amorphization effect on the Li^+ conductivity of Li_3PO_4 from other factors of potential influence, like the condensation of PO_4 tetrahedra into P_2O_7 dimers, which would be promoted by O deficiencies, or the presence of excess Li and isolated O in the structure.

The calculated MSD vs time shows the Li^+ diffusivity in a- Li_3PO_4 to be clearly higher than in γ - Li_3PO_4 . Figure S2 compares Li^+ MSD vs t plots in a- Li_3PO_4 and γ - Li_3PO_4 at 1000 K as an example. However, a- Li_3PO_4 is still too poor a conductor to allow to confidently estimate its room-temperature conductivity using AIMD trajectories of a few tens of picoseconds. The RMSD of Li^+ ions in a- Li_3PO_4 , averaged over intervals of 30 ps, gets through the distance between first Li–Li neighbors (centered at about 3 Å) only by raising T to 1000 K, at which the RMSD ≈ 4 Å and the diffusion of Li^+ is still quite sluggish. Moreover, at higher temperatures the Li^+ self-diffusivity displays a nonlinear behavior as is sometimes observed in polymeric or amorphous materials near the glass transition.⁵⁵ Given the complexity of the case, we rely on the difference between a- Li_3PO_4 and γ - Li_3PO_4 in the calculated Li^+ MSD vs t as indicator of higher ionic mobility in a- Li_3PO_4 —being also supported by the above-mentioned, previously reported experimental and theoretical data—and investigate below the structural variations that can justify such a difference.

3.1.1. Structural Density. The pair distribution function (PDF) computed for the DFT-relaxed model of a- Li_3PO_4 is shown in Figure S3 along with the corresponding structure

function of the scattering vector \vec{Q} , $S(\vec{Q})$. Our amorphous lithium phosphate, a- Li_3PO_4 , has a density $\rho_a = 2.0$ g/cm³, which falls within the uncertainty associated with the experimental value measured by Kuwata et al.,⁴⁹ i.e., 2.2 ± 0.2 g/cm³. ρ_a is $\sim 20\%$ lower than the density of γ - Li_3PO_4 (2.4 g/cm³), and it has been suggested that such a more “open structure” of the amorphous phase might partially account for the increment in Li-ion conductivity.⁵⁶

3.1.2. Geometry and Connectivity of PO_4 Tetrahedra. Similarly to γ - Li_3PO_4 , the structure of a- Li_3PO_4 is characterized by isolated PO_4 units with almost regular tetrahedral geometry. Figure S4 compares P–P and P–O partial PDFs of the DFT optimized structures of a- Li_3PO_4 and γ - Li_3PO_4 . From the P–P PDF plots it is seen that P atoms in a- Li_3PO_4 are separated by a minimum distance over about 4 Å, just as in the crystal phase. The P–O PDF plots show a perfect match between amorphous and crystal phases on the first P–O neighbors distance centered around 1.7 Å. Moreover, a- Li_3PO_4 shows a OPO angle distribution of $109.4 \pm 2.5^\circ$, which is very close to the value of $109.5 \pm 0.5^\circ$ in γ - Li_3PO_4 . These data indicate that a- Li_3PO_4 is made of PO_4 units forming regular tetrahedra.

3.1.3. Orientational Correlation between PO_4 Tetrahedra. One major difference between a- Li_3PO_4 and γ - Li_3PO_4 lies in the orientational correlation between the PO_4 tetrahedra as obtained following the classification proposed by Rey.⁵⁷ A pair of regular PO_4 tetrahedra can be classified according to the number of O atoms that fall in between two parallel planes passing through the P centers and perpendicular to the line joining them. One PO_4 group might expose a corner (1O), an edge (2O), or a face (3O) toward the other PO_4 tetrahedron, and this generates six possible pair combinations: corner-to-corner (1:1), corner-to-edge (1:2), corner-to-face (1:3), edge-to-edge (2:2), edge-to-face (2:3), and face-to-face (3:3).

Figure 3 plots distance-dependent fractions of each of the six classes in a- Li_3PO_4 and γ - Li_3PO_4 , sampled with a spacing of 1 Å. The amorphous phase reveals some short-range orientational order signaled by distinct fluctuations at distances $r < 7$ Å, while at larger distances the random orientation (disorder) limit is approached. Similarly to the crystal phase, a- Li_3PO_4

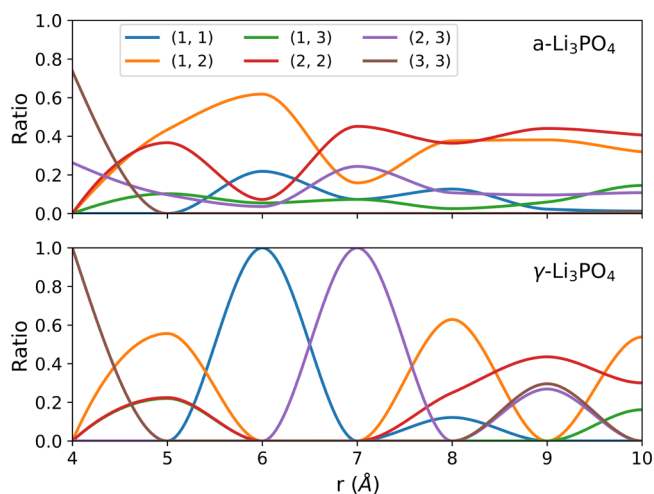


Figure 3. Orientational correlation between PO_4 tetrahedra in a- Li_3PO_4 and crystalline γ - Li_3PO_4 . Different curves represent different configurations of PO_4 pairs: corner-to-corner (1:1), face-to-face (3:3), corner-to-face (1:3), edge-to-edge (2:2), edge-to-face (2:3), and corner-to-edge (1:2).

displays a clear prevalence of face-to-face orientations at very short r , followed by edge-to-face orientations. The weight of face-to-face and edge-to-face configurations drops rather quickly between 4 and 5 Å distance, while 2:2 and 1:2 configurations increase to account for about 40% of the PO_4 pairs each. At 6 Å the most probable configuration is corner-to-edge, and this completes the shell of first P–P neighbors represented by a broad peak between about 4 and 6 Å in the corresponding partial PDF of Figure S4. For distances $r \geq 7$ Å the amplitude of the oscillations fades, and the 2:2 configuration becomes prevalent with about 40% of the PO_4 pairs as analytically predicted for random orientations.⁵⁷

3.1.4. Li Coordination Environment. The orientational disorder of the tetrahedra in the amorphous phase $\text{a-Li}_3\text{PO}_4$ creates significant differences in the average environment of Li^+ as compared to the crystal case. Figures 4a and 4b compare

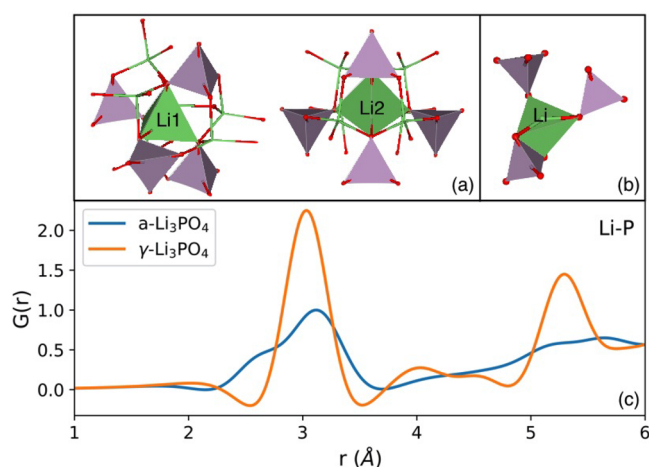


Figure 4. Li coordination environments in (a) $\gamma\text{-Li}_3\text{PO}_4$ and (b) $\text{a-Li}_3\text{PO}_4$. The crystal form, $\gamma\text{-Li}_3\text{PO}_4$, has two independent Li sites (labeled as Li1 and Li2), each being coordinated by four O atoms from as many PO_4 units. In the amorphous case, a large fraction of LiO_4 tetrahedra shares one edge with a PO_4 unit as shown in (b). The lower panel (c) shows the Li–P partial PDF calculated for amorphous and crystalline Li_3PO_4 phases.

typical Li coordination environments in $\gamma\text{-Li}_3\text{PO}_4$ and $\text{a-Li}_3\text{PO}_4$, respectively. The crystalline structure shows two distinct Li sites, both of tetrahedral LiO_4 type. Similarly, in the DFT-optimized structure of $\text{a-Li}_3\text{PO}_4$, Li is mainly found in pseudotetrahedral coordination by O atoms, the average coordination number calculated from a Voronoi analysis⁵⁸ being about 4. For the sake of simplicity, from now on we will refer to the Li coordination polyhedra in $\text{a-Li}_3\text{PO}_4$ as to LiO_4 tetrahedra, even though we note that there are individual sites in the amorphous structure that appear to be either under- or overcoordinated.

A significant difference between $\gamma\text{-Li}_3\text{PO}_4$ and $\text{a-Li}_3\text{PO}_4$ lies in the P distribution around Li. In fact, while in $\gamma\text{-Li}_3\text{PO}_4$ the four O atoms surrounding Li come from as many PO_4 units, the DFT optimized structure of $\text{a-Li}_3\text{PO}_4$ displays more than 70% of its LiO_4 tetrahedra sharing one edge with PO_4 units. By comparison between the partial Li–P PDF of $\gamma\text{-Li}_3\text{PO}_4$ and $\text{a-Li}_3\text{PO}_4$ reported in Figure 4c, it is seen that the edge-sharing between LiO_4 and PO_4 tetrahedra in $\text{a-Li}_3\text{PO}_4$ places Li^+ and P^{5+} in closer proximity to each other. Based on Pauling's rule on the instability of edge-sharing (and face-sharing) polyhedra in ionic compounds,⁵⁹ such a proximity would induce a

destabilization of the Li sites that might contribute to the conductivity improvement in $\text{a-Li}_3\text{PO}_4$ over $\gamma\text{-Li}_3\text{PO}_4$.

To obtain an estimate of the energy difference between edge-sharing and crystal-like Li sites, we calculated the difference between the energies required for the extraction of Li atoms from various sample positions in $\text{a-Li}_3\text{PO}_4$. For each Li atom removal, we performed a single-point energy calculation (without geometry optimization to avoid substantial cell restructuring) and found that the extraction of Li from edge-sharing sites is generally favored by an energy difference that may vary from ~ 50 meV to >1 eV. This indicates that edge-sharing Li sites are destabilized compared to crystal-like Li sites and therefore potentially more mobile. In addition, undercoordinated and overcoordinated Li sites may also be destabilized over crystal-like sites by as much as 1 eV.

The differences in Li^+ coordination environment between $\text{a-Li}_3\text{PO}_4$ and $\gamma\text{-Li}_3\text{PO}_4$ are maintained also during the AIMD simulations. Figure 5 displays statistical pictures of the

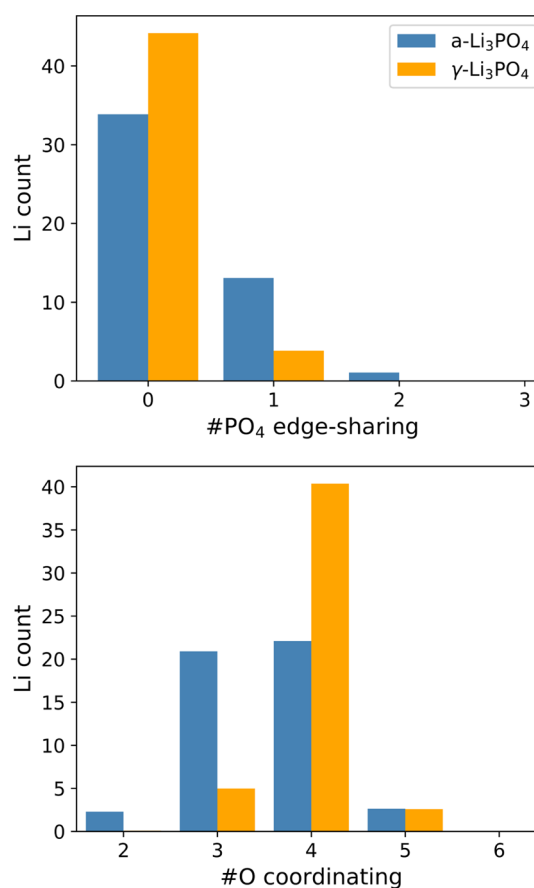


Figure 5. Statistical averages calculated for $\text{a-Li}_3\text{PO}_4$ and $\text{a-Li}_{3.25}\text{PO}_4$ over sample trajectories of 10 ps at 1000 K. The upper panel shows the average amount of LiO_4 – PO_4 edge-sharing within a maximum Li–P distance of 2.7 Å. The lower panel displays the average number of O atoms coordinating Li within a distance of 2.5 Å.

corresponding Li coordination environments along sample trajectories of 10 ps at 1000 K. The top panel shows the average amount of edge-sharing between LiO_4 and PO_4 tetrahedra, whereas the bottom panel reports the average number of O atoms coordinating Li within a 2.5 Å distance, which roughly encloses the first Li–O neighbors as seen from the partial Li–O PDFs in Figure S5. It is seen that substantially more edge-sharing (about 20% of the Li content) and

undercoordinated Li ions (above 40%) are present in α - Li_3PO_4 than in γ - Li_3PO_4 . Similar amounts of edge-sharing and of undercoordinated Li ions in α - Li_3PO_4 are verified for multiple sample trajectories starting at different points along the simulation time and spanning over different time lengths (see Figure S6). This result indicates that Li ions of the amorphous phase are found within an average coordination environment that is more destabilizing than the one in the crystal phase.

3.2. Effect of Excess Li. To evaluate the effect of excess Li on the ionic conductivity of amorphous lithium phosphate without structural modifications from the charge compensating dopant (e.g., N^{3-}), we have introduced about 8% excess Li^+ in the model structure for α - Li_3PO_4 , generating amorphous nonstoichiometric α - $\text{Li}_{3.25}\text{PO}_4$. Excess Li ions were inserted into α - Li_3PO_4 at low energy empty sites identified through Voronoi analysis and classical interatomic potential site energy evaluation and compensated by a uniformly charged background for subsequent DFT geometry optimization. The uniform background charge is a technique commonly adopted for charged defect calculations in DFT.^{60,61} The same procedure was also used to run subsequent AIMD diffusivity simulations.

The calculated MSD vs time reveals a greater mobility of the Li^+ ions in α - $\text{Li}_{3.25}\text{PO}_4$ with respect to stoichiometric α - Li_3PO_4 . In fact, α - $\text{Li}_{3.25}\text{PO}_4$ shows an average Li^+ displacement within a 30 ps time window which exceeds the distance between nearest Li neighbors (see the partial Li–Li PDF in Figure S7) already at 900 K, $\text{RMSD} \approx 4.2$ Å, whereas at 1000 K the average distance covered by Li^+ in 30 ps surpasses 6 Å. This difference in Li^+ mobility between stoichiometric α - Li_3PO_4 and α - $\text{Li}_{3.25}\text{PO}_4$ may be attributed to the fact that α - $\text{Li}_{3.25}\text{PO}_4$ has a larger number of potential charge carriers, but closer analysis suggests an additional, more subtle role of the excess Li in affecting both structure and ionic mobility.

The relaxed Li-excess structure has a density $\rho_{\text{a,ex}} = 2.3$ g/cm³, which is higher than the density of stoichiometric α - Li_3PO_4 , so that one might exclude the above-mentioned “open structure” factor for improving Li-ion diffusion. On the other hand, the combination of the higher structural density and Li content of α - $\text{Li}_{3.25}\text{PO}_4$ yields a distinction in the density of nearest Li–Li neighbors with respect to α - Li_3PO_4 (Figure S7). Figure 6 shows that the average number of Li neighbors within

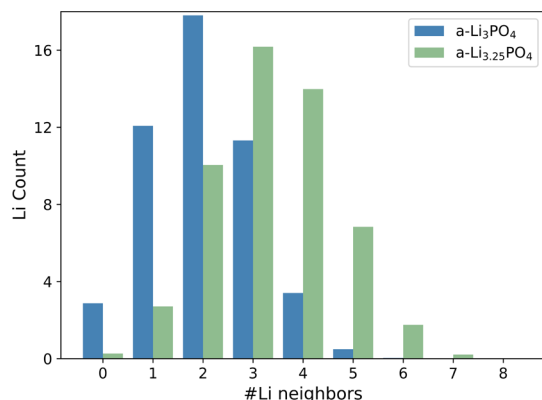


Figure 6. Average Li–Li neighbors density distributions calculated for α - Li_3PO_4 and α - $\text{Li}_{3.25}\text{PO}_4$ over sample trajectories of 10 ps at 1000 K. Li neighbors were selected within a sphere of radius 3.0 Å around each Li.

3 Å distance around each Li increases from 2 in α - Li_3PO_4 to 3 in α - $\text{Li}_{3.25}\text{PO}_4$. The presence of a larger number of short-range Li–Li interactions in the system with excess Li might contribute to increase the average energy of the Li sites and thus enhance the Li^+ mobility.

3.3. Effect of N Doping. An example of a calculated amorphous LiPON structure is shown in Figure 7, with some

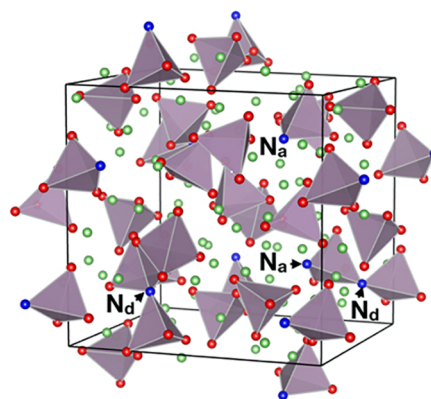


Figure 7. Example of amorphous LiPON structure of composition $\text{Li}_{2.94}\text{PO}_{3.50}\text{N}_{0.31}$ obtained from AIMD simulations. Li (green), P (gray), O (red), N (blue); $\text{P}(\text{O,N})_4$ tetrahedra are drawn. Examples of N atoms in N_a and N_d configurations are highlighted.

apex-substituted N (N_a) and some double bridging N (N_d) highlighted. No triple bridging N (N_t) is ever observed in our amorphous structures. Only in one case ($\text{Li}_{2.69}\text{PO}_{3.38}\text{N}_{0.31}$) did the simulated annealing lead to a structure containing a P–O–P bridge.

Arrhenius plots of the Li-ion diffusivity calculated for the different amorphous LiPON structures are shown in Figure S8. From the σ values reported in Table 1 it is seen that in accordance with experimental observations the conductivity of N-containing amorphous structures is generally higher than the conductivity of α - Li_3PO_4 , though there is considerable variation depending on how N is substituted.

Below we investigate first the relative energies of the different N configurations observed in the amorphous LiPON structures and then the effect of these N structures on the coordination environment and local interactions of Li ions, so as to uncover their influence on the Li-ion mobility. We find that the diffusion of Li^+ is favored by bridging N_d configurations, which however compete with the increase in charge carriers provided by N_a substitutions. Moreover, the energetically favored N_d condensation can cause the release of isolated O anions in the structure, which will be shown to slow down the movement of neighboring Li ions.

3.3.1. Formation Energies of N_a and N_d Configurations. In section 2.3 we have identified three possible N for O substitutions in Li_3PO_4 . The significant reduction of both Li and anion content implied by substitutions of type 3 makes these substitutions unlikely in LiPON thin films, which have typical compositions close to the orthophosphate stoichiometry. This observation is in line with the absence of triple N bridges in our model structures. Instead, substitutions of type 1 and 2 maintain the ratio $\text{Li}:\text{P} \approx 3$ and may be favored over each other depending on the composition (i.e., Li excess or deficiencies, anions to P ratio) and the associated “defect” energy.

For a more quantitative characterization of the energetics of formation of N_a and N_d , we have built a DFT phase diagram (Figure 8) including N-doped near-ground-state phosphate

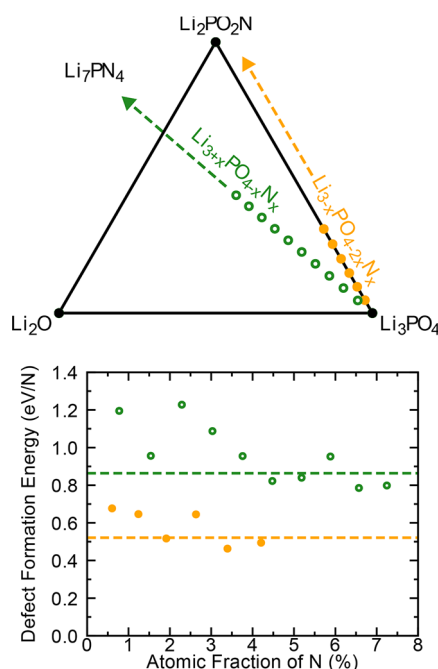


Figure 8. DFT phase diagram for LiPON near-ground-state crystal structures with N_a (green points) and N_d (orange points) defects as identified with the GA-MLP method. All defected structures lie above the hull; i.e., they are thermodynamically unstable and eventually decompose into Li_3PO_4 , Li_2PNO_2 , and Li_2O . Defect formation energies corresponding to such decompositions are plotted in the right panel, showing that N_d defects are energetically favored with respect to N_a defects.

structures identified using the GA-MLP method to sort through a number of possible candidates. Charge-balanced N_a defects were introduced in crystalline Li_3PO_4 by substitution of $[N + Li]^{2-}$ for O^{2-} along the Li_3PO_4 – Li_7PN_4 binary (green points); N_d defects were generated by substituting N^{3-} for $[2O + Li]^{3-}$ along the Li_3PO_4 – Li_2PNO_2 binary (orange points). In each case, both atomic positions and lattice parameters were relaxed at the DFT level of theory. Defect formation energies are defined with respect to the competing equilibria:

$$E_f(N_a) = E(Li_{3+x}PO_{4-x}N_x) - (1-x)E(Li_3PO_4) - xE(Li_2PNO_2) - xE(Li_2O)$$

$$E_f(N_d) = E(Li_{3-x}PO_{4-2x}N_x) - (1-x)E(Li_3PO_4) - xE(Li_2PNO_2)$$

where the DFT minimum-energy structures of crystalline Li_3PO_4 ($Pnma$), Li_2PO_2N ($Cmc2_1$), and Li_2O ($Fm\bar{3}m$) have been used. A plot of the calculated formation energies is shown in the lower panel of Figure 8.

Comparison between $E_f(N_a)$ and $E_f(N_d)$ shows that N_d type configurations are generally favored over N_a by a few hundred meV, which is in agreement with the trend previously reported by Du and Holzwarth²⁶ although the scale of the energy difference is much smaller in our case. The reason for such

discrepancy is due to the fact that Du and Holzwarth²⁶ adopted a model of constant stoichiometry for both defects, which implies that the substitution of O with N_a is accompanied by the formation of a P–O–P bridge as an additional defect in the same structure. Anyways, the relatively small difference between the calculated $E_f(N_a)$ and $E_f(N_d)$ makes both N_a and N_d likely accessible via the magnetron sputtering process used to synthesize LiPON thin films, which involves temperatures of the order of thousands of K and colliding particles with kinetic energies between hundreds of eV and several keV.⁶²

3.3.2. Structural Density and Li Coordination Environment. As expected given their amorphous character, all the calculated LiPON structures display edge-sharing between $Li(O,N)_4$ and $P(O,N)_4$ tetrahedra to an extent that ranges from about 20% to nearly 40% of the relative Li sites (averages over 10 ps sample trajectories at 1000 K). In addition, an average amount of around 30–50% of the Li sites is found to be under- or overcoordinated. We note that the highest percentages of $Li(O,N)_4$ – $P(O,N)_4$ edge-sharing and of under- or overcoordinated Li sites are associated with the most conductive structure here studied, i.e., $Li_{2.94}PO_{3.50}N_{0.31}$. Correspondingly, structures with reduced conductivity like $Li_{3.31}PO_{3.69}N_{0.31}$ and $Li_{3.38}PO_{3.62}N_{0.38}$ are characterized by the lowest deviations from a crystal-like Li-ion environment, which signals also a lower degree of amorphization.

Density values obtained after full geometry optimization of the amorphous LiPON structures range from 2.04 g/cm³ ($Li_{2.69}PO_{3.38}N_{0.31}$) to 2.33 g/cm³ ($Li_{2.94}PO_{3.50}N_{0.31}$) (see Table 1) to be compared with an average density of 2.3 g/cm³ measured for a typical LiPON thin film.⁶³ Most of these structural densities are higher than the density of stoichiometric α - Li_3PO_4 , which again excludes the amorphous “open structure” factor as being decisive for enhancing the ionic conductivity in LiPON electrolytes.

Instead, it appears that the density of the structure rather relates to the density of nearest Li–Li neighbors (see the corresponding partial PDFs in Figure S10 for reference). Figure 9 shows a histogram of the amount of Li ions that can be found within 3 Å distance from a given Li^+ for $Li_{2.69}PO_{3.38}N_{0.31}$ and $Li_{2.94}PO_{3.50}N_{0.31}$. The first compound has a density close to α - Li_3PO_4 (2.0 g/cm³) while the density

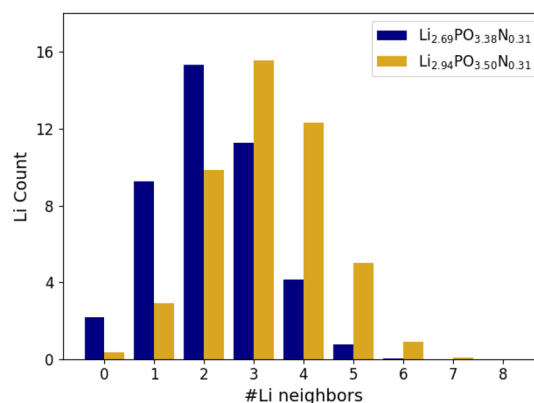


Figure 9. Average Li–Li neighbors density distributions calculated for LiPON structure models of compositions $Li_{2.69}PO_{3.38}N_{0.31}$ and $Li_{2.94}PO_{3.50}N_{0.31}$ over sample trajectories of 10 ps at 1000 K. Li neighbors were selected within a sphere of radius 3.0 Å around each Li.

of the second compound is comparable to the Li-excess α - $\text{Li}_{3.25}\text{PO}_4$ (2.3 g/cm^3). Analogously to what was shown in Figure 6, the two normal distributions in Figure 9 are shifted with respect to each other: the mean value is ~ 2 for $\text{Li}_{2.69}\text{PO}_{3.38}\text{N}_{0.31}$ while it is ~ 3 for $\text{Li}_{2.94}\text{PO}_{3.50}\text{N}_{0.31}$. The other LiPON structures are close to the latter in both density and average number of close Li–Li neighbors.

The tendency of N to form bridges between phosphate groups promotes the condensation of the structure inducing a compaction effect. This compensates for Li deficiencies in $\text{Li}_{2.69}\text{PO}_{3.38}\text{N}_{0.31}$ and particularly in $\text{Li}_{2.94}\text{PO}_{3.50}\text{N}_{0.31}$. In addition, a compaction effect on the phosphate structure is seen also where N doping introduces excess Li, as confirmed by the example of $\text{Li}_{3.38}\text{PO}_{3.62}\text{N}_{0.38}$ in which no N bridges are formed. The greater structural density of LiPON compounds leads to a higher short-range density of Li–Li neighbors, which might contribute to the increased mobility of the Li ions and therefore also to the increase in conductivity with respect to α - Li_3PO_4 .

3.3.3. Local Interactions of Li Ions with N and Phosphate O. We have analyzed local Li–N and Li–O interactions in terms of how strongly the anions act to confine the movement of Li ions. We get a measure of the strength of the local interactions between Li and a given atom X by measuring the time Li^+ remains in the neighborhood of X (here defined as a sphere of radius $r = 2.5 \text{ \AA}$ centered around X) once it has entered there.

We refer to Li^+ entering the sphere of influence of X as an “event” and focus on $\text{Li}_{2.94}\text{PO}_{3.50}\text{N}_{0.31}$, which is the structure with highest conductivity among those investigated. We have calculated the fractions of events that happen during an AIMD simulation of 30 ps at 1000 K around the five different N atoms in its unit cell, i.e., 2 N_a and 3 N_d .

At a delay time $t = 30 \text{ ps}$, the van Hove correlation function defined in eq 6 shows maxima at about 5 \AA and above (see Figure S9), meaning that, with a high probability, a Li ion has already traveled a distance $r \geq 5 \text{ \AA}$ in 30 ps. Because a distance of 5 \AA is well beyond the nearest-neighbor distance between Li (about 2.8 \AA , see the Li–Li partial PDF in Figure S10), we can consider the events happening in this time window as being independent of each other. Figure 10 (top panel) plots the fraction of events happening around N atoms in $\text{Li}_{2.94}\text{PO}_{3.50}\text{N}_{0.31}$ as a function of simulation time. It is seen that N_d shows lower anchoring power on Li^+ than N_a and thus smoothes the Li-ion mobility: about 80% of the events around N_d lasts less than 0.2 ps, whereas it can take more than 0.5 ps for the same amount of events to happen around N_a , the results being quite consistent within each group of N. Note that the average number of events is roughly the same for N_a (396) and N_d (360), but the sum of the times of all events is on average more than doubled for N_a (132 ps) vs N_d (53 ps). Average residence times of Li^+ at the different N sites are therefore about 0.33 ps for N_a and 0.15 ps for N_d .

The difference in anchoring power between N_a and N_d might be explained by the fact that N_d has saturated its atomic valence forming covalent P–N and P=N bonds that reduce its electron charge (7.112 – $7.147e$, as obtained from Bader analysis⁶⁴ on the DFT optimized structure using a $160 \times 168 \times 168$ grid) with respect to N_a (7.154 – $7.162e$) and thus interacts less strongly with Li^+ than N_a . Moreover, the presence of two phosphate groups near N_d adds a steric encumbrance factor which reduces the space for the interactions with Li^+ . Figure 10 (bottom panel) shows that N_d attracts Li^+ less

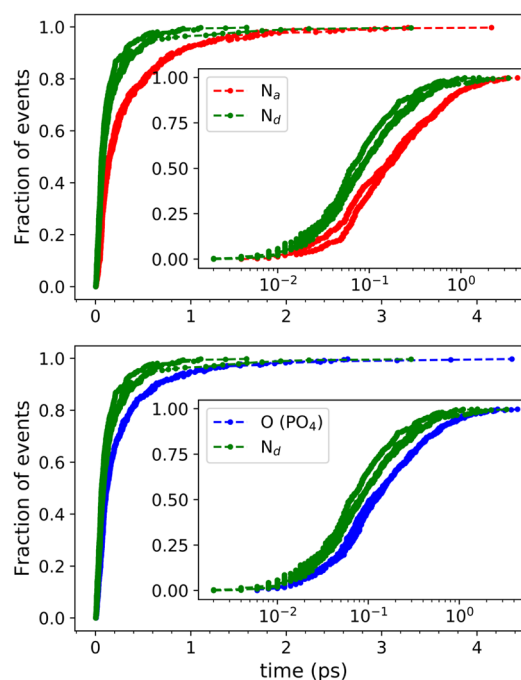


Figure 10. Fraction of events happening around N and O atoms in $\text{Li}_{2.94}\text{PO}_{3.50}\text{N}_{0.31}$ during a simulation time of 30 ps at 1000 K (semilogarithmic plot in the inset). An event is defined as one Li ion entering a sphere of radius $r = 2.5 \text{ \AA}$ (sphere of influence) around the atom. The top panel compares different types of N: there are 2 N_a and 3 N_d species in the structure, represented in red and green, respectively. The bottom panel compares N_d atoms (green) with phosphate O atoms (blue).

strongly also than regular phosphate O, as expected from the higher electronegativity of the latter. In contrast, no significant difference is found between N_a and O.

Therefore, in agreement with the electrostatic argument presented in section 1, we confirm that N_d bridges favor the mobility of Li ions in LiPON electrolytes due to the formation of strong covalent bonds between P and N that reduce the overall attraction exerted on Li^+ . This finding explains the relatively low value of σ for $\text{Li}_{3.38}\text{PO}_{3.62}\text{N}_{0.38}$, as it is the only amorphous LiPON model in our investigation which does not display N_d species (only N_a). We find no evidence that the presence of N_d bridges establishes preferential pathways for the migration of Li^+ . This is probably because N bridging condensation is generally limited to pairs (or at most triplets) of phosphate units and does not create the extended phosphate chains that would be needed to achieve percolation along N_d bridges.

3.3.4. Presence of Isolated O. An additional important factor relating to N insertion in lithium phosphate is the possible formation of isolated O anions in the structure. Isolated O, namely O^{2-} not covalently bonded to any P, is distinguished as being surrounded only by Li^+ and not being bonded to any P within a distance $r < 2 \text{ \AA}$, which comprises intratetrahedral P–O distances (see for instance the first neighbors peak in the partial P–O PDF in Figure S4). When the (O + N):P ratio is kept fixed at 4, the tendency of N to form N_d bridges can create isolated O^{2-} anions during the simulated annealing. This was observed in our amorphous model for $\text{Li}_{3.31}\text{PO}_{3.69}\text{N}_{0.31}$: within a cell of 133 atoms, 5 of which are N, 2 N_d bridges are formed and as many isolated O

released as shown in Figure S11. In the case of $\text{Li}_{3.31}\text{PO}_{3.69}\text{N}_{0.31}$, the isolated O anions formed in an AIMD melt-and-quench process during an equilibration period of 80–90 ps at 3000 K and exist thereafter over a time scale of about 102 ps, corresponding to the overall simulation time of the applied stepwise cooling procedure. They are also maintained by the DFT structure relaxation performed at the end of the AIMD simulation.

To understand whether isolated O and O in regular phosphate units affect the Li^+ mobility differently, we have monitored their local interactions. Figure 11 compares the

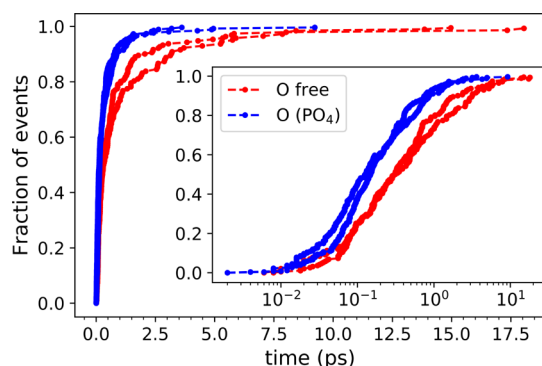


Figure 11. Fraction of events happening within a cutoff distance of 2.5 Å around the two isolated O atoms in $\text{Li}_{3.31}\text{PO}_{3.69}\text{N}_{0.31}$ during a simulation time of 30 ps at 1000 K (semilogarithmic plot in the inset). Comparison with as many regular phosphate O atoms in the same structure is made. Isolated O and phosphate O are represented in red and blue, respectively.

statistical time that Li^+ resides in the neighborhood of isolated O (red) and phosphate O (blue) during a sample AIMD simulation of 30 ps at 1000 K. The isolated O are essentially stationary (their displacements along the trajectory vary between 0.5 and 0.9 Å) and clearly exert greater constraint on the migration of the Li^+ than normal phosphate O. Hence, isolated O embedded in the structure has a negative effect on the Li^+ mobility, and this explains the relatively low conductivity of $\text{Li}_{3.31}\text{PO}_{3.69}\text{N}_{0.31}$. A similar effect of suppression of Li^+ migration has been attributed also to isolated S anions in $\text{Li}_2\text{S}-\text{P}_2\text{S}_5$ glass electrolytes.⁶⁵

Further indirect proof that isolated O^{2-} suppresses the ionic conductivity was obtained by calculating σ for a modified $\text{Li}_{3.31}\text{PO}_{3.69}\text{N}_{0.31}$ structure where the isolated O are removed as either (i) Li_2O or (ii) O^{2-} anions (with background charge balance). In case (i) σ turns out to be lower (2.0×10^{-8} S/cm), presumably due to the lower Li content, which further supports the importance of excess Li; in case (ii), instead, σ is increased to 5.9×10^{-5} S/cm.

4. DISCUSSION

Because of their outstanding electrochemical resistance and reasonably high room-temperature Li-ion conductivity, LiPON electrolytes have been widely used in thin-film batteries. Despite the importance of these materials and the numerous reports on the subject, no mechanistic understanding has been established in the literature. In this paper we bridge this gap using *ab initio* molecular dynamics simulations on well-controlled and characterized LiPON models to determine the effect of both structural features (i.e., amorphization, bridging and nonbridging N configurations) and compositional

factors (Li content, anions to P ratio, presence of isolated O) on the Li^+ conductivity.

The same models served also in a separate work⁶³ to solve the challenging task of characterizing the amorphous structure of LiPON. Indeed, comparisons with neutron scattering and infrared experiments reveal excellent agreement, further supporting the validity of the present results.

A first outcome from our research is that the amorphization of the Li_3PO_4 structure improves the conductivity, even without compositional modifications. This is due to the induced modification of the Li environment. The orientational disorder of the PO_4 tetrahedra smooths the potential energy surface for the diffusion of Li^+ ions by destabilizing a number of Li sites. A statistical analysis (Figure 5) shows that a non-negligible fraction (>20%) of Li^+ polyhedra shares an edge with PO_4 , which destabilizes the Li^+ site due to the greater proximity between Li^+ and P^{5+} . Moreover, numerous Li sites are found to be either under- or overcoordinated, which further contributes to increasing their energy, thus lowering the activation barrier for the Li^+ migration. Notably, Du and Holzwarth⁵³ have shown that a major obstacle to Li^+ diffusion in crystalline $\gamma\text{-Li}_3\text{PO}_4$ is the formation of vacancy–interstitial pair defects: a considerable energy input ($E_f \approx 1.7$ eV) is required to displace one Li ion from the deep potential well where it sits in the crystal, whereas migration barriers can be as low as 0.3 eV.

The idea that a portion of Li ions is mobilized by a destabilizing coordination environment agrees with the observation made by Fleutot et al.⁵⁴ through ^7Li NMR measurements that only a fraction of the Li content in LiPON electrolytes is effectively mobile and participates in the conduction mechanism.

Another factor that promotes the Li^+ mobility is the excess Li that can be introduced via N doping (reaction 1 in section 2.3). Du and Holzwarth⁵³ recognized that excess Li is the best extrinsic mobile species in crystalline $\gamma\text{-Li}_3\text{PO}_4$ as it triggers a concerted mechanism of interstitial diffusion. For amorphous LiPON electrolytes, the results reported in this work show that the impact of excess Li on the ionic conductivity goes beyond the well-known proportionality relationship between σ and carrier concentration. We found that independently of the identity of the dopant element, excess Li leads to a compaction of the phosphate structure which increases the average short-range density of Li–Li neighbors (Figure 6). The interactions among close Li^+ neighbors augment the destabilizing effect of polyhedral edge-sharing and nonideal coordination of the Li sites and thus presumably increase the number of mobile charge carriers.

This puts amorphous LiPON in an interesting category of ionic conductors where the conductivity increases with density, contrary to the common idea that larger volume and “open space” is beneficial for mobility. The latter hypothesis is indeed valid for conductors where mobility is limited by the size of a bottleneck through which the ion has to migrate, as is the case for a lot of crystalline compounds with low concentration of the diffusing ions (e.g., spinels).⁶⁶ Indeed, a high mobility Mg^{2+} solid electrolyte was recently developed by increasing the volume of the spinel structure through the use of large anions and cations.⁶⁷ LiPON does not seem to be “bottleneck-limited”, probably due to its amorphous nature; rather, the conductivity of LiPON benefits from the increased Li–Li interaction resulting from a smaller volume. One would expect the Li–Li interaction effect to increase in importance for

compounds with high Li content, as is the case of many superionic Li conductors such as $\text{Li}_7\text{P}_3\text{S}_{11}$, $\text{Li}_{10}\text{GeP}_2\text{S}_{12}$, LiZnPS_4 , etc.

Despite the beneficial effect of excess Li on the ionic mobility, one might argue that the experimental observations for LiPON,^{4,10} as reported in Table 1, point to Li-deficient situations as being those that deliver the highest conductivities. In this regard, we notice that the application of the concept of off-stoichiometry to amorphous systems is somewhat questionable given their existence in a continuous compositional range. For practical reasons, the composition of an amorphous system can be compared to the stoichiometry of a related crystalline compound, but the designation of Li-excess or Li-deficient will naturally depend on the choice of the reference compound. The phase diagram in Figure 1 shows that the references against which one compares the Li content for $\text{Li}_x\text{PO}_y\text{N}_z$ can in principle vary between metaphosphate ($x = 1$) and orthophosphate stoichiometry ($x = 3$), passing through the intermediate case of pyrophosphate $\text{Li}_4\text{P}_2\text{O}_7$ ($x = 2$). A composition with $2 < x < 3$ would be Li-deficient when referenced to orthophosphate Li_3PO_4 but Li-excess when referenced to pyrophosphate $\text{Li}_4\text{P}_2\text{O}_7$ or to metaphosphate LiPO_3 .

The combination of data reported for phosphorus oxynitride bulk glasses^{9,15} with measurements on LiPON thin-film electrolytes^{4,10,11,54} reveals a nonlinear trend of the ionic conductivity as a function of the Li content. The conductivity σ increases with the Li amount and reaches a maximum for a ratio Li:P slightly below 3. Indeed, one of the highest conductivities so far reported for LiPON thin films is found for the composition $\text{Li}_{2.9}\text{PO}_{3.3}\text{N}_{0.46}$ ^{4,10} (see Table 1). This nonlinear behavior is successfully reproduced by our amorphous LiPON models and can now be understood in light of the analysis performed in the present work: as the Li content increases, the relative weight of the concentration of charge carriers on the conductivity decreases and is counterbalanced by a structural factor connected with the incorporation of N_d bridges between phosphate units. In fact, from the reactions listed in section 2.3, it is seen that the insertion of excess Li in LiPON structures corresponds to $1(\text{N}^{3-}):1(\text{O}^{2-})$ substitutions generating N_a and competes with the formation of N_d bridges. The latter were found to be energetically favored over N_a configurations and are beneficial for the mobility of Li^+ , in agreement with experimental work^{11,54} suggesting that the enhancement of the conductivity caused by N is due to structural modifications of the phosphate framework rather than to an increase in Li content.

Our analysis shows that although the formation of N_d bridges is accompanied by a reduction of the Li content, it can increase the ionic conductivity. This is explained by two mechanisms: (1) the corresponding increase of the structural density, which destabilizes Li^+ sites through increased short-range Li–Li interactions, and (2) the increase of the N-covalency. The latter is consistent with our finding that the cumulative time of events where Li is anchored near N_d is shorter than for N_a or phosphate O, meaning that the saturated valence state of N_d , involved in strongly covalent bonds with P, diminishes its electrostatic interactions with Li^+ , thus promoting the mobility of neighboring Li ions. The optimum balance between Li and N_d contents is achieved for $\text{Li}_{2.94}\text{PO}_{3.50}\text{N}_{0.31}$, which has a “Li-deficient” composition favoring phosphates condensation via N_d bridges and yet maintains a relatively high Li concentration. This model

displays Li:P and (O + N):P ratios very close to those of the best performing LiPON sample reported in Table 1.

In general, assuming that all N enters the original Li_3PO_4 structure by replacing O, the following equation is satisfied for $\text{Li}_x\text{PO}_y\text{N}_z$:

$$y = 4 - f_{\text{O}_\text{r}} = 4 - z(2f_{\text{N}_\text{d}} + f_{\text{N}_\text{a}})$$

where f_{O_r} is the fraction of replaced O, and f_{N_d} and f_{N_a} are the fractions of N in double-bridging and apical configuration, respectively. On the basis of this simple arithmetic relationship, we can conjecture that slightly more than half of the N present in Yu et al.'s⁴ sample $\text{Li}_{2.9}\text{PO}_{3.3}\text{N}_{0.46}$ is in the form of N_d , which can explain its high conductivity despite the small Li deficiency with respect to Li_3PO_4 . The same reasoning explains why a Li-excess sample such as $\text{Li}_{3.1}\text{PO}_{3.8}\text{N}_{0.16}$ ⁴ (see Table 1) has lower conductivity compared to the previous case, as only about 25% of the total amount of N is accommodated in the form of N_d .

Fleutot et al.⁵⁴ also found an increase in conductivity of LiPON samples with N content, despite the Li content being reduced. In this case we note that the less conductive compositions reported by these authors indicate the presence of abundant excess Li. In view of the tendency of N to form N_d bridges, the high anion content that accompanies excess Li, i.e., $y + z \approx 4$, increases the probability of releasing isolated O anions in the structure, which we have shown to slow down the migration of Li^+ . Therefore, we speculate that the relatively low conductivity of Fleutot et al.'s⁵⁴ LiPON samples is due to the presence of isolated O^{2-} embedded in their structure.

5. CONCLUSION

In this work we used *ab initio* molecular dynamics simulations to generate amorphous LiPON structure models and investigate the mechanisms of ion conductivity in LiPON electrolytes. In-depth analysis of structures and diffusivities allowed us to relate conductivity trends to (1) amorphization, (2) presence of excess Li, and (3) structural changes due to N substitution. Calculated LiPON structures display N_d bridges and apical N configurations, whereas no triple N bridges between P atoms were found. Our results show that several factors contribute to the Li-ion conductivity of LiPON:

1. The orientational disorder of the PO_4 polyhedral units in the amorphous structure creates edge-sharing between LiO_4 and PO_4 tetrahedra as well as under- or overcoordinated Li^+ , which in turn increases the Li site energy.
2. Increased Li–Li interactions caused by excess Li from a $1(\text{N}^{3-}):1(\text{O}^{2-})$ substitution, and by densification from bridging N_d , can also increase the energy of Li sites, enhancing the Li^+ mobility.
3. N-bridging condensation of phosphate units lowers the electrostatic interaction between Li^+ and the anions.

Finally, we find that the presence of isolated O anions in structures with excess Li, and hence with high anion content (ratio (O + N):P \approx 4), can reduce the mobility of neighboring Li ions. On the basis of these findings, we conclude that to maximize the Li^+ mobility in LiPON it is important to accommodate N in bridging sites while keeping a high concentration of charge carriers, which implies that the concentration of excess Li with respect to Li_3PO_4 and of isolated O anions should be minimized.

■ ASSOCIATED CONTENT

■ Supporting Information

The Supporting Information is available free of charge on the ACS Publications website at DOI: [10.1021/acs.chemmater.8b02812](https://doi.org/10.1021/acs.chemmater.8b02812).

ANN potential error distribution and performance relative to the DFT reference; MSD versus time plots of amorphous and crystalline Li_3PO_4 at 1000 K; pair distribution and scattering structure functions calculated for a- Li_3PO_4 ; P–P, P–O, and Li–O partial PDFs of a- Li_3PO_4 ; percentages of LiO_4 – PO_4 edge-sharing and Li–O coordination in a- Li_3PO_4 over different time windows; Li–Li partial PDFs calculated for a- Li_3PO_4 and a- $\text{Li}_{3.25}\text{PO}_4$; Arrhenius plots of the LiPON diffusivities; van Hove self-correlation function of Li ions in $\text{Li}_{2.94}\text{PO}_{3.50}\text{N}_{0.31}$; comparison of Li–Li first-neighbors PDF peaks in a- Li_3PO_4 and the different LiPON models; view of the $\text{Li}_{3.31}\text{PO}_{3.69}\text{N}_{0.31}$ structure model (PDF)

■ AUTHOR INFORMATION

Corresponding Authors

*E-mail: vlacivita@lbl.gov (V.L.).

*E-mail: gceder@berkeley.edu (G.C.).

ORCID

Valentina Lacivita: 0000-0002-2800-4471

Nongnuch Artrith: 0000-0003-1153-6583

Notes

The authors declare no competing financial interest.

■ ACKNOWLEDGMENTS

The information, data, or work presented herein was funded in part by the Advanced Research Projects Agency - Energy (ARPA-E), U.S. Department of Energy, Award DE-AR0000775. In addition, this work was supported by the U.S. Department of Energy, Office of Science, Basic Energy Sciences, Materials Sciences and Engineering Division under Contract DE-AC02-05-CH11231. This research used resources of the National Energy Research Scientific Computing (NERSC) Center, a DOE Office of Science User Facility supported by the Office of Science of the U.S. Department of Energy under Contract DE-AC02-05CH11231. Computational resources were provided also by Extreme Science and Engineering Discovery Environment (XSEDE), which was supported by National Science Foundation Grant ACI-1053575. V.L. thanks Dr. Murathan Aykol (currently at the Toyota Research Institute, California, United States) and Dr. Marco De La Pierre (now at the Pawsey Supercomputing Centre, Perth, Australia) for helpful technical discussions on AIMD simulations and Dr. Andrew S. Westover and Dr. Nancy J. Dudney (at Oak Ridge National Laboratory, TN) for valuable discussions on LiPON electrolytes.

■ REFERENCES

- (1) Bates, J. B.; Dudney, N. J.; Gruzalski, G. R.; Zuhr, R. A.; Choudhury, A.; Luck, C. F.; Robertson, J. D. Electrical properties of amorphous lithium electrolyte thin films. *Solid State Ionics* **1992**, 53–56, 647–654.
- (2) Bates, J. B.; Lubben, D.; Dudney, N. J.; Hart, F. X. 5 V Plateau in LiMn_2O_4 Thin Films. *J. Electrochem. Soc.* **1995**, 142, L149–L151.
- (3) Wang, B.; Bates, J. B.; Hart, F. X.; Sales, B. C.; Zuhr, R. A.; Robertson, J. D. Characterization of Thin-Film Rechargeable Lithium

Batteries with Lithium Cobalt Oxide Cathodes. *J. Electrochem. Soc.* **1996**, 143, 3203–3213.

(4) Yu, X.; Bates, J. B.; Jellison, G. E.; Hart, F. X. A Stable Thin-Film Lithium Electrolyte: Lithium Phosphorus Oxynitride. *J. Electrochem. Soc.* **1997**, 144, 524–532.

(5) Dudney, N. J. Solid-state thin-film rechargeable batteries. *Mater. Sci. Eng., B* **2005**, 116, 245–249.

(6) Marchand, R. Nitrogen-containing phosphate glasses. *J. Non-Cryst. Solids* **1983**, 56, 173–178.

(7) Reidmeyer, M. R.; Rajaram, M.; Day, D. E. Preparation of phosphorus oxynitride glasses. *J. Non-Cryst. Solids* **1986**, 85, 186–203.

(8) Larson, R. W.; Day, D. E. Preparation and characterization of lithium phosphorus oxynitride glass. *J. Non-Cryst. Solids* **1986**, 88, 97–113.

(9) Wang, B.; Kwak, B. S.; Sales, B. C.; Bates, J. B. Ionic conductivities and structure of lithium phosphorus oxynitride glasses. *J. Non-Cryst. Solids* **1995**, 183, 297–306.

(10) Bates, J. B.; Dudney, N. J.; Gruzalski, G. R.; Zuhr, R. A.; Choudhury, A.; Luck, C. F.; Robertson, J. D. Fabrication and characterization of amorphous lithium electrolyte thin films and rechargeable thin-film batteries. *J. Power Sources* **1993**, 43, 103–110.

(11) Roh, N.-S.; Lee, S.-D.; Kwon, H.-S. Effects of deposition condition on the ionic conductivity and structure of amorphous lithium phosphorus oxynitrate thin film. *Scr. Mater.* **1999**, 42, 43–49.

(12) Jacke, S.; Song, J.; Dimesso, L.; Brötz, J.; Becker, D.; Jaegermann, W. Temperature dependent phosphorous oxynitride growth for all-solid-state batteries. *J. Power Sources* **2011**, 196, 6911–6914.

(13) Marchand, R.; Agliz, D.; Boukbir, L.; Quemerais, A. Characterization of nitrogen containing phosphate glasses by X-ray photoelectron spectroscopy. *J. Non-Cryst. Solids* **1988**, 103, 35–44.

(14) Day, D. E. Structural role of nitrogen in phosphate glasses. *J. Non-Cryst. Solids* **1989**, 112, 7–14.

(15) Muñoz, F.; Durán, A.; Pascual, L.; Montagne, L.; Revel, B.; Martins Rodrigues, A. C. Increased electrical conductivity of LiPON glasses produced by ammonolysis. *Solid State Ionics* **2008**, 179, 574–579.

(16) Muñoz, F. Comments on the structure of LiPON thin-film solid electrolytes. *J. Power Sources* **2012**, 198, 432–433.

(17) Carrette, B.; Ribes, M.; Souquet, J. L. The effects of mixed anions in ionic conductive glasses. *Solid State Ionics* **1983**, 9–10, 735–737.

(18) Magistris, A.; Chiodelli, G.; Duclot, M. Silver borophosphate glasses: Ion transport, thermal stability and electrochemical behaviour. *Solid State Ionics* **1983**, 9–10, 611–615.

(19) Tatsumisago, M.; Yoneda, K.; Machida, N.; Hinami, T. Ionic conductivity of rapidly quenched glasses with high concentration of lithium ions. *J. Non-Cryst. Solids* **1987**, 95–96, 857–864.

(20) Wang, B.; Chakoumakos, B. C.; Sales, B. C.; Kwak, B. S.; Bates, J. B. Synthesis, crystal structure, and ionic conductivity of a polycrystalline lithium phosphorus oxynitride with the γ - Li_3PO_4 structure. *J. Solid State Chem.* **1995**, 115, 313–323.

(21) Unuma, H.; Sakka, S. Electrical conductivity in Na-Si-O-N oxynitride glasses. *J. Mater. Sci. Lett.* **1987**, 6, 996–998.

(22) Unuma, H.; Komori, K.; Sakka, S. Electrical conductivity and chemical durability in alkali-silicate oxynitride glasses. *J. Non-Cryst. Solids* **1987**, 95–96, 913–920.

(23) Anderson, O. L.; Stuart, D. A. Calculation of Activation Energy of Ionic Conductivity in Silica Glasses by Classical Methods. *J. Am. Ceram. Soc.* **1954**, 37, 573–580.

(24) Du, Y. A.; Holzwarth, N. A. W. Effects of O vacancies and N or Si substitutions on Li^+ migration in Li_3PO_4 electrolytes from first principles. *Phys. Rev. B: Condens. Matter Mater. Phys.* **2008**, 78, 174301.

(25) Du, Y. A.; Holzwarth, N. A. W. First principles simulations of Li ion migration in materials related to LiPON electrolytes. *ECS Trans.* **2009**, 25, 27–36.

- (26) Du, Y. A.; Holzwarth, N. A. W. First-principles study of LiPON and related solid electrolytes. *Phys. Rev. B: Condens. Matter Mater. Phys.* **2010**, *81*, 184106.
- (27) Guille, E.; Vallverdu, G.; Baraille, I. First-principle calculation of core level binding energies of $\text{Li}_x\text{PO}_y\text{N}_z$ solid electrolyte. *J. Chem. Phys.* **2014**, *141*, 244703.
- (28) Guille, E.; Vallverdu, G.; Tison, Y.; Bégué, D.; Baraille, I. Possible Existence of a Monovalent Coordination for Nitrogen Atoms in $\text{Li}_x\text{PO}_y\text{N}_z$ Solid Electrolyte: Modeling of X-ray Photoelectron Spectroscopy and Raman Spectra. *J. Phys. Chem. C* **2015**, *119*, 23379–23387.
- (29) Blöchl, P. E. Projector augmented-wave method. *Phys. Rev. B: Condens. Matter Mater. Phys.* **1994**, *50*, 17953.
- (30) Perdew, J. P.; Burke, K.; Ernzerhof, M. Generalized Gradient Approximation Made Simple. *Phys. Rev. Lett.* **1996**, *77*, 3865–3868.
- (31) Kresse, G.; Furthmüller, J. Efficient iterative schemes for ab initio total-energy calculations using a plane-wave basis set. *Phys. Rev. B: Condens. Matter Mater. Phys.* **1996**, *54*, 11169.
- (32) Basconi, J. E.; Shirts, M. R. Effects of Temperature Control Algorithms on Transport Properties and Kinetics in Molecular Dynamics Simulations. *J. Chem. Theory Comput.* **2013**, *9*, 2887–2899.
- (33) Martínez, L.; Andrade, R.; Birgin, E. G.; Martínez, J. M. PACKMOL: A package for building initial configurations for molecular dynamics simulations. *J. Comput. Chem.* **2009**, *30*, 2157–2164.
- (34) Juhás, P.; Farrow, C. L.; Yang, X.; Knox, K. R.; Billinge, S. J. L. Complex modeling: a strategy and software program for combining multiple information sources to solve ill posed structure and nanostructure inverse problems. *Acta Crystallogr., Sect. A: Found. Adv.* **2015**, *71*, S62–S68.
- (35) Momma, K.; Izumi, F. VESTA3 for three-dimensional visualization of crystal, volumetric and morphology data. *J. Appl. Crystallogr.* **2011**, *44*, 1272–1276.
- (36) Gomer, R. Diffusion of adsorbates on metal surfaces. *Rep. Prog. Phys.* **1990**, *53*, 917–1002.
- (37) Uebing, C.; Gomer, R. Determination of surface diffusion coefficients by Monte Carlo methods: Comparison of fluctuation and Kubo–Green methods. *J. Chem. Phys.* **1994**, *100*, 7759–7766.
- (38) Kowsari, M. H.; Alavi, S.; Najafi, B.; Gholizadeh, K.; Dehghanpisheh, E.; Ranjbar, F. Molecular dynamics simulations of the structure and transport properties of tetra-butylphosphonium amino acid ionic liquids. *Phys. Chem. Chem. Phys.* **2011**, *13*, 8826–8837.
- (39) Howard, J.; Hood, Z. D.; Holzwarth, N. A. W. Fundamental aspects of the structural and electrolyte properties of Li_2OHCl from simulations and experiment. *Phys. Rev. Mater.* **2017**, *1*, 075406.
- (40) Ong, S. P.; Richards, W. D.; Jain, A.; Hautier, G.; Kocher, M.; Cholia, S.; Gunter, D.; Chevrier, V. L.; Persson, K. A.; Ceder, G. Python Materials Genomics (pymatgen): A robust, open-source python library for materials analysis. *Comput. Mater. Sci.* **2013**, *68*, 314–319.
- (41) Mo, Y.; Ong, S. P.; Ceder, G. First Principles Study of the $\text{Li}_{10}\text{GeP}_2\text{S}_{12}$ Lithium Super Ionic Conductor Material. *Chem. Mater.* **2012**, *24*, 15–17.
- (42) Ong, S. P.; Mo, Y.; Richards, W. D.; Miara, L.; Lee, H. S.; Ceder, G. Phase stability, electrochemical stability and ionic conductivity of the $\text{Li}_{10\pm1}\text{MP}_2\text{X}_{12}$ ($\text{M} = \text{Ge, Si, Sn, Al}$ or P , and $\text{X} = \text{O, S}$ or Se) family of superionic conductors. *Energy Environ. Sci.* **2013**, *6*, 148–156.
- (43) Van Hove, L. Correlations in Space and Time and Born Approximation Scattering in Systems of Interacting Particles. *Phys. Rev.* **1954**, *95*, 249–262.
- (44) Artrith, N.; Urban, A.; Ceder, G. Constructing first-principles phase diagrams of amorphous Li_xSi using machine-learning-assisted sampling with an evolutionary algorithm. *J. Chem. Phys.* **2018**, *148*, 241711.
- (45) Artrith, N.; Urban, A. An implementation of artificial neural-network potentials for atomistic materials simulations: Performance for TiO_2 . *Comput. Mater. Sci.* **2016**, *114*, 135–150.
- (46) Artrith, N.; Urban, A.; Ceder, G. Efficient and accurate machine-learning interpolation of atomic energies in compositions with many species. *Phys. Rev. B: Condens. Matter Mater. Phys.* **2017**, *96*, 014112.
- (47) Senevirathne, K.; Day, C. S.; Gross, M. D.; Lachgar, A.; Holzwarth, N. A. W. A new crystalline LiPON electrolyte: Synthesis, properties, and electronic structure. *Solid State Ionics* **2013**, *233*, 95–101.
- (48) Kuwata, N.; Iwagami, N.; Matsuda, Y.; Tanji, Y.; Kawamura, J. Thin Film Batteries with Li_3PO_4 Solid Electrolyte Fabricated by Pulsed Laser Deposition. *ECS Trans* **2008**, *16*, 53–60.
- (49) Kuwata, N.; Lu, X.; Miyazaki, T.; Iwai, Y.; Tanabe, T.; Kawamura, J. Lithium diffusion coefficient in amorphous lithium phosphate thin films measured by secondary ion mass spectroscopy with isotope exchange methods. *Solid State Ionics* **2016**, *294*, 59–66.
- (50) Kuwata, N.; Iwagami, N.; Tanji, Y.; Matsuda, Y.; Kawamura, J. Characterization of thin-film lithium batteries with stable thin-film Li_3PO_4 solid electrolytes fabricated by ArF excimer laser deposition. *J. Electrochem. Soc.* **2010**, *157*, A521–A527.
- (51) Ivanov-Shitz, A. K.; Kireev, V. V.; Mel'nikov, O. K.; Demianets, L. N. Growth and ionic conductivity of $\gamma\text{-Li}_3\text{PO}_4$. *Crystallogr. Rep.* **2001**, *46*, 864–867.
- (52) Li, W.; Ando, Y.; Minamitani, E.; Watanabe, S. Study of Li atom diffusion in amorphous Li_3PO_4 with neural network potential. *J. Chem. Phys.* **2017**, *147*, 214106.
- (53) Du, Y. A.; Holzwarth, N. A. W. Mechanisms of Li^+ diffusion in crystalline γ - and $\beta\text{-Li}_3\text{PO}_4$ electrolytes from first principles. *Phys. Rev. B: Condens. Matter Mater. Phys.* **2007**, *76*, 174302.
- (54) Fleutot, B.; Pecquenard, B.; Martinez, H.; Letellier, M.; Levasseur, A. Investigation of the local structure of LiPON thin films to better understand the role of nitrogen on their performance. *Solid State Ionics* **2011**, *186*, 29–36.
- (55) Angell, C. A.; Ngai, K. L.; McKenna, G. B.; McMillan, P. F.; Martin, S. W. Relaxation in glassforming liquids and amorphous solids. *J. Appl. Phys.* **2000**, *88*, 3113–3157.
- (56) Swenson, J.; Börjesson, L. Correlation between Free Volume and Ionic Conductivity in Fast Ion Conducting Glasses. *Phys. Rev. Lett.* **1996**, *77*, 3569–3572.
- (57) Rey, R. Quantitative characterization of orientational order in liquid carbon tetrachloride. *J. Chem. Phys.* **2007**, *126*, 164506.
- (58) O'Keeffe, M. A proposed rigorous definition of coordination number. *Acta Crystallogr., Sect. A: Cryst. Phys., Diff., Theor. Gen. Crystallogr.* **1979**, *35*, 772–775.
- (59) Pauling, L. The principles determining the structure of complex ionic crystals. *J. Am. Chem. Soc.* **1929**, *51*, 1010–1026.
- (60) Van de Walle, C. G.; Neugebauer, J. First-principles calculations for defects and impurities: Applications to III-nitrides. *J. Appl. Phys.* **2004**, *95*, 3851–3879.
- (61) Freysoldt, C.; Grabowski, B.; Hickel, T.; Neugebauer, J.; Kresse, G.; Janotti, A.; Van de Walle, C. G. First-principles calculations for point defects in solids. *Rev. Mod. Phys.* **2014**, *86*, 253–305.
- (62) Kim, B.-C. Sputtering deposition apparatus and method utilizing charged particles. Patent US5840167A, 1998.
- (63) Lacivita, V.; Westover, A. S.; Kercher, A.; Phillip, N. D.; Yang, G.; Veith, G.; Ceder, G.; Dudney, N. J. Resolving the amorphous structure of lithium phosphorus oxynitride (Lipon). *J. Am. Chem. Soc.* **2018**, *140*, 11029–11038.
- (64) Tang, W.; Sanville, E.; Henkelman, G. A grid-based Bader analysis algorithm without lattice bias. *J. Phys.: Condens. Matter* **2009**, *21*, 084204.
- (65) Baba, T.; Kawamura, Y. Structure and Ionic Conductivity of $\text{Li}_2\text{S-P}_2\text{S}_5$ Glass Electrolytes Simulated with First-Principles Molecular Dynamics. *Front. Energy Res.* **2016**, *4*, 22.
- (66) Wang, Y.; Richards, W. D.; Ong, S. P.; Miara, L. J.; Kim, J. C.; Mo, Y.; Ceder, G. Design principles for solid-state lithium superionic conductors. *Nat. Mater.* **2015**, *14*, 1026–1031.

(67) Canepa, P.; Bo, S.-H.; Gopalakrishnan, S. G.; Key, B.; Richards, W. D.; Shi, T.; Tian, Y.; Wang, Y.; Li, J.; Ceder, G. High magnesium mobility in ternary spinel chalcogenides. *Nat. Commun.* **2017**, *8*, 1759.